Applied Catalysis B: Environmental 127 (2012) 234–245

Contents lists available at SciVerse ScienceDirect

Applied Catalysis B: Environmental

journal homepage: www.elsevier.com/locate/apcatb

Influence of cerium modification methods on catalytic performance of Au/mordenite catalysts in CO oxidation

Lei Qi[a], Changjin Tang[a], Lei Zhang[a], Xiaojiang Yao[a], Yuan Cao[a], Lichen Liu[a], Fei Gao[b,*], Lin Dong[a,b,*], Yi Chen[a]

[a] Key Laboratory of Mesoscopic Chemistry of MOE, School of Chemistry and Chemical Engineering, Nanjing University, Nanjing 210093, PR China
[b] Jiangsu Key Laboratory of Vehicle Emissions Control, Center of Modern Analysis, Nanjing University, Nanjing 210093, PR China

ARTICLE INFO

Article history:
Received 1 May 2012
Received in revised form 6 August 2012
Accepted 14 August 2012
Available online 23 August 2012

Keywords:
Mordenite
Au
Ce modification
Synergistic effect
CO oxidation

ABSTRACT

This work investigated influence of cerium modification methods (impregnation and ion-exchange) on the gold dispersion, surface chemical states, synergistic effect between gold and cerium and CO oxidation activity of Au catalysts supported on Ce modified mordenites. The supports and catalysts were characterized by XRF, ICP, XRD, N_2 adsorption–desorption, UV–vis spectroscopy, HRTEM, in situ FT-IR and XPS. In general, Ce-containing Au catalysts were found to be more active in CO oxidation than the Ce-free counterpart, with the impregnation method of cerium modification being more effective than the ion exchange method. The different catalytic performance of Ce-containing catalysts was related to multiple factors: (1) the impregnation method of cerium modification was more favorable to form Au particles with smaller mean size than the ion-exchange method, due to the higher ratio of surface Lewis acid sites; (2) the interface between Au and CeO_2 particles produced by impregnation method was more beneficial for the redox equilibrium of $Au^0 + Ce^{4+} \leftrightarrow Au^{3+} + Ce^{3+}$ to shift to right to form more active Au^{3+} species than the interface between Au particles and Ce cations produced by ion-exchange method, which enhanced the synergistic effect between gold and cerium and the catalytic performance of CO oxidation.

1. Introduction

Since Haruta and co-workers found that CO oxidation could be achieved at a low temperature if gold nanoparticles were formed on suitable supports [1,2], catalysis by gold nanoparticles has attracted much attention because of their high activity. Previous studies have demonstrated that the nature of support plays a significant role in the stabilization and dispersion of the active phase [3]. Furthermore, the reducible metal oxide support can supply reactive oxygen to the active gold sites in the reaction process [4]. From this point of view, it is of great importance to investigate the interaction between gold nanoparticle and the support.

Recently, with the advantages of its adjustable acidic property [5], zeolite has been used as a superior support for loading gold nanoparticles [6]. Mohamed et al. [7] prepared the dealuminated and nondealuminated mordenite to support gold, and found that the dealuminated support was responsible for the stability of CO coordinated Au^+. Wan et al. [8] adjusted surface acidity of Y-type zeolite prior to the preparation of gold catalysts. They found that the gold particles on the surface acidity modified Y support are smaller and more uniformly distributed than those on the support without any surface pretreatment. In the light of these literatures, the distribution, charge and stability of the gold species supported on the zeolite depend on the concentration and strength of acid centers of the zeolite [8]. Modification of zeolite by different metal ions, such as Fe, Ce and Ti [8–10], is one of the methods of improvement of acidic property of zeolite, stabilization of gold species and catalytic performance of supported gold catalysts. Among these additives, due to the unique properties of ceria, such as high oxygen storage capacity and well redox cycles between Ce^{3+} and Ce^{4+} [11], ceria has become one of the most interesting active oxide materials employed for the modification of gold catalysts. Some studies demonstrated that the use of cerium to modify zeolite could increase oxygen mobility in the oxidation reaction and improve reaction activity [9,12]. However, little information on the Au catalysts supported on cerium modified mordenite has been reported. Other than these, the role of interface between gold and cerium species has been regarded as adsorption and reaction sites for CO

* Corresponding authors at: School of Chemistry and Chemical Engineering, Nanjing University, Hankou Road 22#, Nanjing, Jiangsu 210093, PR China.
Tel.: +86 25 83592290; fax: +86 25 83317761.
E-mail addresses: gaofei@nju.edu.cn (F. Gao), donglin@nju.edu.cn (L. Dong).

0926-3373/$ – see front matter © 2012 Elsevier B.V. All rights reserved.
http://dx.doi.org/10.1016/j.apcatb.2012.08.013

oxidation [3]. Several theoretical studies have shown that O_2 can be absorbed at the gold–cerium interface and that the reaction barrier for CO oxidation is very low at the interface [13,14]. Liu et al. [15] proposed that a charge transfer from Au atom to a neighboring Ce cation would occur during the catalysis process, which promoted the reaction. Flytzani-Stephanopoulos et al. [16] recently studied the CO oxidation reaction on a well-controlled Au/CeO_2 multilayered structure (called nanotower), and found that the reaction rate scaled with the total length of the Au/CeO_2 interface for nanotowers with the same total Au and CeO_2 surface areas. Thus, different morphologies and properties of gold–cerium interfaces can lead to distinct catalytic activities. However, to our knowledge, little attention has been paid to comparing the effect of different gold–cerium interfaces, i.e. interface between Au and CeO_2 particles or between Au particles and Ce cations, on the synergistic effect and catalytic performance. Modification of mordenite with cerium by different methods can in turn provide different cerium species, such as CeO_2 particles and Ce ions [9], which is a suitable route to investigate this effect.

In this work, supported Au mordenite catalysts were modified with Ce by impregnation and ion-exchange methods to obtain different gold–cerium interfaces. The as-prepared Au catalysts were characterized by means of XRF, ICP, XRD, UV–vis, N_2 adsorption–desorption, HRTEM, XPS, in situ FT-IR and CO oxidation model reaction. This study mainly focuses on the influences of difference support surfaces on the dispersion, dimension and charge of Au particles, and the contribution from different gold–cerium interfaces to the catalytic properties of CO oxidation.

2. Experimental

2.1. Catalyst preparation

2.1.1. Preparation of supports

Acid zeolite mordenite (HMOR) with a silicon to aluminum ratio of 7.1 and $Ce(NO_3)_3{\cdot}6H_2O$ were used as received. The Ce-supported material was prepared by incipient wetness impregnation method with $Ce(NO_3)_3$ solution. The CeO_2 loading amount was 3 wt%. The mixture was kept stirring for 3 h and was evaporated at 110 °C. The resultant material was calcined at 500 °C in the flowing air for 5 h. This support was denoted as CeM_{imp}.

Another Ce-containing support was prepared by liquid-phase ion-exchange of HMOR with 0.5 mol L^{-1} $Ce(NO_3)_3$ solution at 80 °C for 6 h. This ion-exchange procedure was carried out twice. After completion of ion-exchange, the sample was washed thoroughly with deionized water and dried overnight at 110 °C. Subsequently, the support was calcined at 500 °C for 5 h in air atmosphere. This support was referred as CeM_{ie}.

2.1.2. Preparation of Au catalysts

The supported Au catalysts were prepared via the deposition–precipitation method using $HAuCl_4{\cdot}4H_2O$ as gold precursor. $HAuCl_4$ solution was added dropwise to a stirred suspension of 1 g support in water. The pH of the solution was kept close to 8.5 with NaOH (0.05 mol L^{-1}), and the solution thermostated at 70 °C was aged for 1 h. The catalyst was washed repeatedly with distilled water, dried in air overnight at 100 °C and calcined at 300 °C for 3 h in flowing air atmosphere. The resulted samples were designated as Au/M, Au/CeM_{imp} and Au/CeM_{ie}, respectively.

2.2. Catalyst characterization

The Si/Al molar ratios and Ce contents of pure supports and Au catalysts were analyzed by X-ray fluorescence spectrometer (ARL-9800).

The actual Au contents of Au catalysts were derived from a Jarrell-Ash 1100 inductively coupling plasma (ICP) atomic emission spectrometer. The samples were completely dissolved in suitable acid before analysis.

XRD patterns were recorded on a Philips X'pert Pro diffractometer using Ni-filtered Cu Kα radiation (0.15418 nm). The X-ray tube was operated at 40 kV and 40 mA. The instrumental line broadening was measured using a silicon standard. The grain sizes of the prepared materials were determined by the Scherrer equation. Lattice volumes of the samples were calculated by full curve fitting, using Jade 5 software.

The total surface areas of these supports and Au catalysts were determined via nitrogen adsorption at −196 °C with the Brunauer–Emmett–Teller (BET) method using a Micrometrics ASAP-2020 apparatus. The surface areas and volumes of micropores were obtained from the *t*-plot method.

UV–vis diffuse reflectance spectra were recorded in the range of 200–900 nm by a Shimadzu UV-2401 spectrophotometer with $BaSO_4$ as reference for baseline emendation. The spectrum of the support was subtracted from the spectrum of the corresponding Au catalyst.

HRTEM images of these samples were obtained by a JEM-2100 microscope at an acceleration voltage of 200 kV, equipped with energy dispersive X-ray spectrometer (EDX).

FT-IR spectra were collected on a Nicolet 5700 FT-IR instrument (Thermo Electron Corporation, USA) with a resolution 4 cm^{-1}. For the transmission IR experiments under ambient condition, the measured wafer was prepared by using KBr as diluent.

In situ FT-IR spectra of ammonia adsorption were collected on a Nicolet 5700 FT-IR instrument. The nature of acid sites was investigated using ammonia as the probe molecule. A thin, but intact, self-supporting wafer (≈15 mg) of the adsorbents was prepared and mounted inside a high temperature cell (HTC-3, Harrick Scientific Corporation, USA). The wafer was pretreated by N_2 (99.999%) at 300 °C for 1 h. After cooling to ambient temperature, NH_3 (99.999%) was introduced into the HTC at atmospheric pressure for 30 min, then the cell was flushed by N_2 for 30 min. After that, the HTC was heated to 300 °C under N_2 atmosphere at a rate of 10 °C min^{-1}, and the spectra were recorded at various target temperatures.

In situ FT-IR spectra of CO adsorption were collected on a Nicolet 5700 FT-IR instrument. The self-supporting wafer mounted in HTC-3 was pretreated for 1 h at 300 °C in the flowing N_2 atmosphere. After cooled to room temperature, the sample was conducted to a controlled stream of 2 vol% CO/N_2 for 30 min. In situ CO adsorption FT-IR spectra were recorded at various target temperatures with subtraction of the corresponding background reference.

X-ray photoelectron spectroscopy (XPS) analysis was performed on a PHI5000 Versaprobe high performance electron spectrometer, using Al Kα radiation (1486.6 eV) operating at an accelerating power of 25 W. All binding energies (BE) were referenced to the C 1s peak at 284.6 eV to account for the charging effect. This reference gave BE values with an accuracy at ±0.1 eV.

2.3. Catalytic activity measurements

The CO oxidation activities of Au catalysts were measured in a flow micro-reactor with a gas composition of 1.6 vol% CO, 20.8 vol% O_2 and 77.6 vol% N_2 at a space velocity of 30,000 mL g^{-1} h^{-1}, and 50 mg catalyst was used for each measurement. The catalyst was pretreated in a N_2 stream at 200 °C for 1 h and then cooled to room temperature, after that, the mixed gases were switched on. Two columns and thermal conductivity detector (TCD) were used for the purpose of analyzing the production, column A with 13× molecular sieve for separating O_2, N_2 and CO, and column B, packed with Porapak Q for separating CO_2.

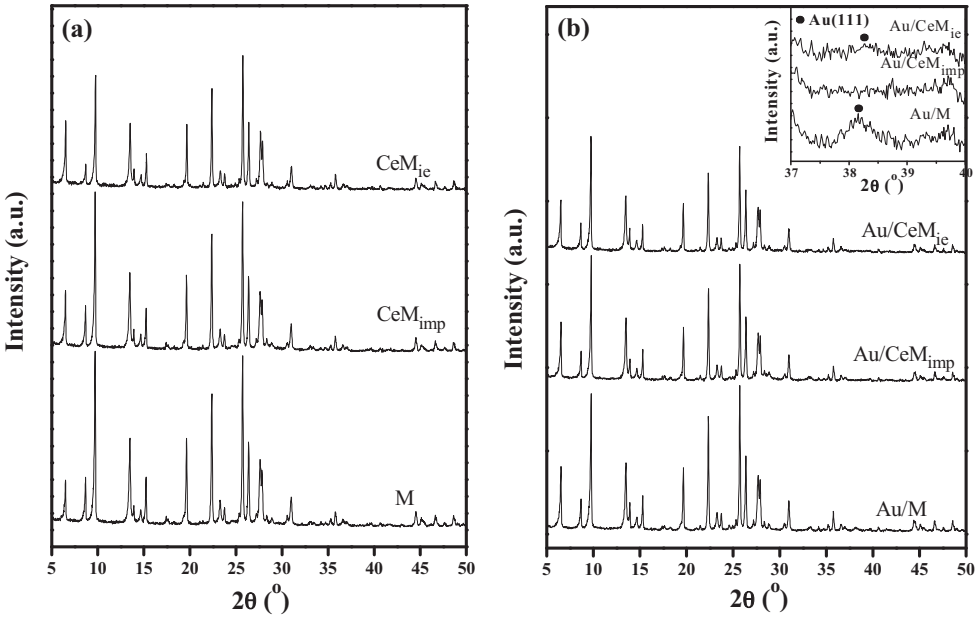

Fig. 1. XRD patterns of (a) supports and (b) Au catalysts.

The CO or O_2 pretreatment of Au catalysts was conducted as follows: first the catalyst was pretreated in a flowing N_2 stream at 200 °C for 1 h, then CO or O_2 stream was switched on and the CO or O_2 pretreatment was carried on at 200 °C for 1 h. The sample pretreated by CO or O_2 was cooled to room temperature in the flowing N_2. After that, the mixed gases were switched on and catalytic activities were measured.

3. Results and discussion

3.1. Chemical composition and textural properties

As shown in Table 1, the Si/Al ratios for all samples are almost same, and Ce contents in Ce-containing ones are similar. Regardless of the similar nominal Au content of the catalysts (0.0051 at.%), chemical analysis shows a relatively large range of the gold loadings (0.0017–0.0035 at.%). The surface atomic ratios of Ce and Au determined by XPS are much higher than the corresponding ratios determined by XRF and ICP (Table 1), indicating the enrichment of Ce and Au species on the mordenite surface. All catalysts were found to be chlorine-free, as confirmed by EDX results discussed below.

The textural characteristics of the investigated zeolitic samples are shown in Table 1. CeM$_{imp}$ and CeM$_{ie}$ supports show lower values of total surface area (S_{BET}), surface area of micropores (S_t^{μ}) and micropore volume (V^{μ}) but little higher average pore radius (r) than those of M one. This finding might indicate that the location of some cerium species in the mordenite pores leads to a surface decrease and an increase of average pore diameter. This existence is expected to block a portion of micropores leading to a measurable decrease in the V^{μ} value and a loss of microporosity. The values of external surface area (S_t^{ext}) of various samples are very small (<5% S_{BET}) attributing to the porous nature of these solids. A comparison of the specific surface area and pore volumes of the pure supports and gold catalysts indicates that the values of S_{BET}, S_t^{μ} and V^{μ} remarkably decrease after the deposition of gold, especially Au/M, due to some blocking of the support micropores with the guest gold particles. The maximum S_{BET} of Au/CeM$_{imp}$ among Au catalysts may origin from the smallest size of Au particles.

3.2. Structure and morphology of supports and Au catalysts

XRD patterns of the pure supports and Au catalysts are displayed in Fig. 1. The diffractograms of CeM$_{imp}$ and CeM$_{ie}$ supports are intact to that of MOR in Fig. 1(a), indicating that the structure of mordenite is maintained even after Ce modification. Additionally, no reflections belonging to cerium oxides are observed in all the Ce-containing samples, suggesting that Ce species are well-dispersed with a particle size lower than the detection limit or are non-crystalline [9]. The observed decrease in the intensities of the diffraction peaks of CeM$_{imp}$ and CeM$_{ie}$ supports may be partly due to an enhanced absorption of X-ray energy in the presence of Ce species, instead of a decrease in crystallinity [17]. The lattice volumes of CeM$_{imp}$ and CeM$_{ie}$ supports are similar to that of pure mordenite (Table 1), indicative of the presence of a major portion of Ce species outside the zeolite framework. Fig. 1(b) shows the XRD patterns of samples after the deposition of gold with low content. A very weak peak at 38.2°, corresponding to the planes (1 1 1) of metal Au [JCPDS (Card No. 84-1286)], appears in Au/M and Au/CeM$_{ie}$ patterns, but is absent in Au/CeM$_{imp}$ one. These results imply that the gold particle size of Au/CeM$_{imp}$ is smaller than that of Au/M and Au/CeM$_{ie}$.

The morphology of supported Au catalysts is exhibited by HRTEM images (Fig. 2(a)–(c)). The size of Au particles on Au/CeM$_{imp}$ and Au/CeM$_{ie}$ samples is much smaller than that on Au/M, which indicates that the introduction of Ce species is favorable for the formation of small gold particles. The average Au particle size follows the trend: Au/CeM$_{imp}$ (5 nm) < Au/CeM$_{ie}$ (8 nm) < Au/M (20 nm) (Fig. 2(d)–(f)). Additionally, in Fig. 2(b) (the insert image), CeO_2 particles can be observed on Au/CeM$_{imp}$, which are absent for Au/CeM$_{ie}$. CeO_2 particles intimately contact with Au particles on Au/CeM$_{imp}$ sample, subsequently forming Au—CeO_2 interface. EDX results (Fig. 2(g)–(i)) could prove the existence of Au and Ce in both Au/CeM$_{imp}$ and Au/CeM$_{ie}$ and only Au in Au/M.

The morphology of Ce species is further studied using FT-IR and UV–vis spectra. Infrared spectra of the zeolite lattice vibrational modes observed between 400 and 1000 cm^{-1} were recorded for the different supports (Fig. 3). As it can be seen, the main bands due to symmetric stretching vibration of T—O (T = Al, Si) belonging to alternate SiO_4 and AlO_4 tetrahedra (at 805 and 750 cm^{-1}) [18],

Table 1
Chemical composition and some structure characteristics of pure supports and Au catalysts.

Sample	Bulk composition[a]			Surface composition[b]			V (Å^3)[c]	S_{BET} ($m^2\,g^{-1}$)[d]	S_t^{μ} ($m^2\,g^{-1}$)[e]	S_t^{ext} ($m^2\,g^{-1}$)[f]	r (Å)[g]	V^{tot} ($cm^3\,g^{-1}$)[h]	V^{μ} ($cm^3\,g^{-1}$)[i]	Microporosity (%)
	Si/Al	Ce (at.%)	Au (at.%)	Si/Al	Ce (at.%)	Au (at.%)								
M	7.1	–	–	12.17	–	–	2750.475	463.2	428.5	34.7	20.0	0.232	0.200	86
CeM_{imp}	7.1	0.017	–	13.43	0.20	–	2745.072	433.0	392.8	40.2	20.8	0.226	0.182	81
CeM_{ie}	7.1	0.019	–	12.91	0.35	–	2749.688	456.9	412.5	44.4	20.6	0.236	0.192	81
Au/M	7.1	–	0.0017	10.95	–	0.06	2768.402	334.9	313.8	21.1	20.3	0.192	0.168	88
Au/CeM_{imp}	7.0	0.017	0.0019	9.69	1.30	0.17	2766.705	428.0	390.6	37.4	21.0	0.217	0.174	80
Au/CeM_{ie}	7.1	0.018	0.0035	9.42	1.06	0.36	2767.142	409.6	376.1	33.5	21.5	0.208	0.167	80

[a] Bulk composition determined by XRF and ICP.
[b] Surface composition determined by XPS.
[c] Lattice volume.
[d] Total surface area determined using BET equation.
[e] Surface area of micropores determined from *t*-plot method.
[f] External surface area of micropores determined from *t*-plot method.
[g] Average pore radius.
[h] The total pore volume at $p/p_0 = 0.97$.
[i] Micropore volume.

Al—O vibration in four-membered rings (at 635 cm^{-1}) [18], and vibration of five-membered rings (at 582 and 563 cm^{-1}) [19] are retained in Ce-containing supports, which reflects the intact structure of mordenite framework following Ce incorporation. However, a new band at 420 cm^{-1}, attributed to Ce—O vibrations in CeO_2 [20], appears in CeM_{imp} support, which is not observed in the spectrum of M and CeM_{ie} ones. This finding can indicate that CeO_2 particles are present in CeM_{imp} support, but are absent in CeM_{ie} one. Furthermore, the existence and coordination of Ce species in mordenite are identified by UV–vis diffuse reflectance spectroscopy. As shown in Fig. 4(a), CeM_{imp} shows two absorption bands at 274 and 314 nm, respectively. The band at 274 nm can be attributed to the electronic transition with charge transfer ($O_2^- \rightarrow Ce^{4+}$) associated to Ce^{4+} ions around SiO_2 [21], and the latter can be assigned to the inter-band transitions taking place in CeO_2 that could be associated with the presence of the Ce^{4+} ions in 8-fold coordination of the fluorite type structure [22]. While CeM_{ie} shows only one band at 274 nm, and M shows neither of these bands. These results indicate that Ce species exist as CeO_2 particles in CeM_{imp}, but Ce^{4+} ions in CeM_{ie}.

UV–vis spectra can provide further evidence for the morphology of Au species. In the UV–vis spectra of Au catalysts (Fig. 4(b)), two kinds of gold species characterized by absorption bands in zone I and II are observed. The bands in zone I manifested at 230–370 nm are typical for Au_n clusters ($1 < n < 10$) [23]. Au/M sample shows no band in zone I. The band wavelength of Au/CeM_{imp} is higher than that of Au/CeM_{ie}. This indicates that the environment around Au clusters of Au/CeM_{imp} is different from that of Au/CeM_{ie}, possibly originating from the adjacency of Au clusters to CeO_2 particles on Au/CeM_{imp} sample. Moreover, the wide bands in zone II are attributed to the surface plasmon resonance of gold nanoparticles [24]. As seen, the latter bands shift to lower wavelength (from 542 to 524 nm) after adding Ce species. There is no simple explanation of this phenomenon because the peak position of surface plasmon resonance is correlated to both particle size and reflective index of supporting materials [25]. However, one needs to have in mind that the Ce species has the potential to alter the local environment of gold, inducing shifts in the position of the bands. Furthermore, the nature of Ce species can vary with the modified methods, providing different environments for gold and leading to different shift of band position.

In order to investigate the cause of different distribution of Au particles on Ce-free and Ce-containing supports, the surface acidic property of supports is studied by in situ FT-IR spectra of ammonia adsorption (Fig. 5). In the spectra of M sample (Fig. 5(a)), the peak at 1435 cm^{-1} ascribed to the asymmetry deformation vibration of ammonia cation NH_4^+ can be detected, which suggests that ammonia is protonated at the Brønsted acid sites of the sample [26]. The peak at 1265 cm^{-1} is attributed to the asymmetric bending vibrations of the N–H bonds in NH_3 coordinately linked to Lewis acid sites [27]. The peak area of ammonia adsorption on Brønsted acid sites is much larger than that on Lewis acid sites, indicating the Brønsted acid sites are the main acid sites on the surface of MOR sample at the same temperature. For CeM_{imp} sample (Fig. 5(b)), it can be seen that the peaks of NH_3 adsorption on Brønsted (ca. 1435 cm^{-1}) and Lewis acid sites (ca. 1265 cm^{-1}) are both obviously observed, indicating that there are abundant Brønsted acid sites as well as Lewis acid sites on the surface of the sample. While the spectra of CeM_{ie} sample (Fig. 5(c)) are similar to those of M support, in which both Brønsted and Lewis acid sites can be detected. The percentage of Lewis acid sites in the total number of acid sites (Brønsted acid sites + Lewis acid sites) on each of the tested samples was estimated from the integrated peak areas of the two bands at 1435 and 1265 cm^{-1} [28]. The percentage of Lewis acid sites follows the order of $CeM_{imp} > CeM_{ie} > M$ in the temperature range 25–300 °C (Fig. 5(d)). This indicates that the ratios of Lewis acid sites

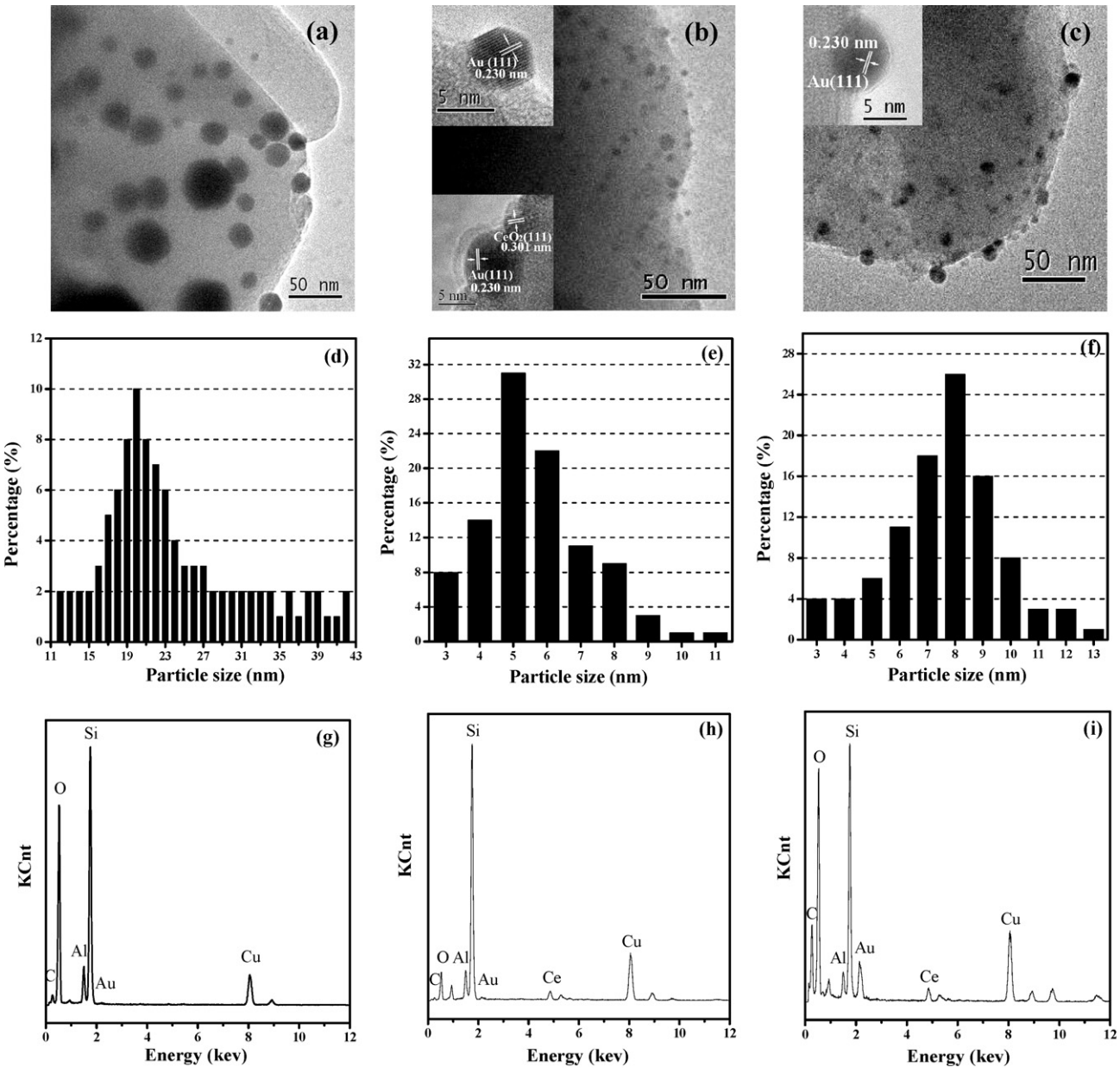

Fig. 2. HRTEM images of (a) Au/M, (b) Au/CeM_{imp} and (c) Au/CeM_{ie}; Au particle size distribution of (d) Au/M, (e) Au/CeM_{imp} and (f) Au/CeM_{ie}; EDX spectra of (g) Au/M, (h) Au/CeM_{imp} and (i) Au/CeM_{ie}.

increase after cerium modification. There are two possible reasons for this result. Firstly, the hydrogen–oxygen bonds of the bridging hydroxyl groups, connecting with Brønsted acidity [29], become less ionic due to the induction of Ce cation and thus Brønsted acid sites decrease [30]. Secondly, because of the existence of an empty f orbit in cerium cation, the amount of Lewis acid would increase [31]. Besides, CeO_2 particles can also provide additional Lewis acid sites attributed to its electron-seeking action [32,33], thus CeM_{imp} support possesses the highest ratio of Lewis acid sites among these mordenite supports. Combined with HRTEM results, the deposited Au particles on CeM_{imp} support are smaller than those on CeM_{ie} and M supports, which is related to the ratio of Lewis acid sites. It is well-known that gold exhibits a high electronegativity and high ionization potential, which make it a poor electron donor [34]. Lewis acid sites originate from electronic vacancies in the structure [35] and such vacancies play an important role in the adsorption and nucleation of gold species [35]. Additionally, previous studies have shown that the surface of CeO_2 particles can easily be enriched with vacancies [14,35], and that gold nucleates exclusively on these vacancies [34]. It is reasonable that Au particles intimately contact with CeO_2 particles and the Au—CeO_2 interface appears for Au/CeM_{imp} sample. Hence, CeM_{imp} support with highest ratio of Lewis acid sites is beneficial to forming Au particles with smallest size.

3.3. *In situ CO-IR spectra results*

In situ FT-IR of CO adsorption was used to gain further insight into the interaction of CO with the Au catalyst surface. For Au/M sample (Fig. 6(a)), the band with two rotational branches, centered at 2360 cm^{-1}, is assigned to gas CO_2 [36]. The intensities of CO_2 bands keep the same with the elevation of temperature. An asymmetry peak at 2055 cm^{-1}, only observed below 75 °C, is associated with CO coordinated to negatively charged Au clusters [37]. Carbonate and formate species can be detected in the range from ca. 2000 to 1400 cm^{-1}, such as organic-like carbonate (1968 and

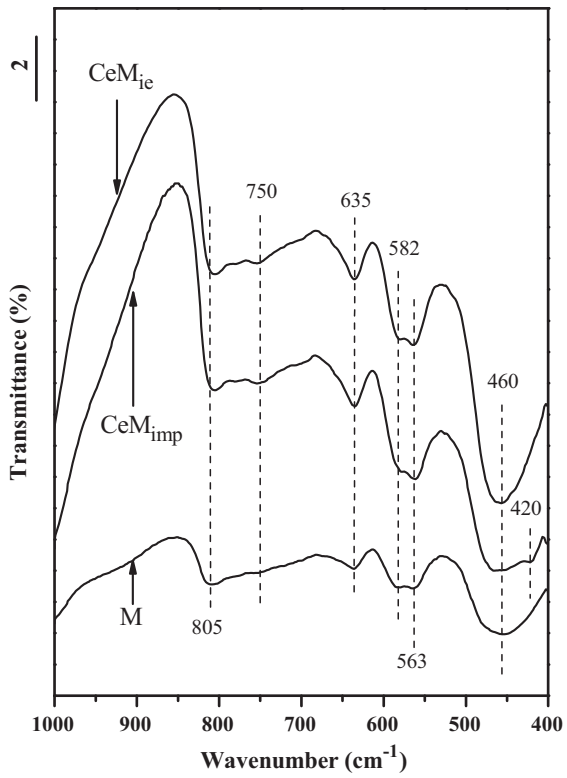

Fig. 3. FT-IR spectra of supports.

1853 cm^{-1}), bridged carbonate (1955 cm^{-1}), unidentate formate (1632 cm^{-1}), carboxylate (1605 cm^{-1}), polydentate (1453 cm^{-1}) and unidentate carbonate (1419 cm^{-1}) [9,37,38]. Some carbonates are very stable even after heat treatment up to 325 °C. For Au/CeM$_{imp}$ and Au/CeM$_{ie}$ samples (Fig. 6(b) and (c)), carboxylate (1605 cm^{-1}) and unidentate carbonate (1419 cm^{-1}) species are absent. CO_2 bands can also be observed, but the intensities change with the increase of temperature. It should be noted that as the band at 1453 cm^{-1} disappears, the intensity of CO_2 peak begins to increase progressively and the peak at 2118 cm^{-1} ascribed to CO–Au^0 appears [36]. It is indicated that the increase of CO_2 is due to desorption or decomposition of carbonates, and subsequently the adsorption sites for CO are exposed. Furthermore, the crucial temperature of polydentate disappearance for Au/CeM$_{imp}$ sample is 200 °C, which is lower than that for Au/CeM$_{ie}$ (250 °C). The carbonate species, blocking the active sites for CO oxidation [39], are easier to disappear for Au/CeM$_{imp}$ than for Au/CeM$_{ie}$, which is an important reason for the activity improvement. In the light of these results, Au/CeM$_{imp}$ sample is expected to show better catalytic performance than Au/M and Au/CeM$_{ie}$ ones.

3.4. Catalytic tests of CO oxidation

CO oxidation reactions were carried out in three consecutive runs over the Au catalysts, as shown in Fig. 7(a). Au/M sample shows little activity in the reaction. For Au/CeM$_{imp}$ sample, the catalytic activity occurs at 50 °C and the complete CO conversion is at 175 °C for the first cycle. The result of the second run is further enhanced with a lower temperature of complete CO conversion at 125 °C. This sample shows a stable catalytic activity when the third catalytic cycle is performed consecutively and the CO conversions at same temperature overlap very well within the experimental error (±10%). For Au/CeM$_{ie}$ sample, the CO conversion at 175 °C is only 28% in the first catalytic run, but it sharply increases to 100% for the second cycle. This sample below 175 °C has a slight deactivation in the third cycle. Moreover, the catalytic activity of CO oxidation in the same cycle over Au/CeM$_{ie}$ sample is lower than that over Au/CeM$_{imp}$ sample, despite there is a higher loading amount of Au for Au/CeM$_{ie}$ sample.

The catalytic activity of CO oxidation is greatly enhanced after Ce modification, and Au/CeM$_{imp}$ exhibits the best catalytic performance in every cycle. The correlation between the average Au particle size and the catalytic response of Au catalysts in CO oxidation is primarily considered. These Ce-containing catalysts perform better than Ce-free one in CO oxidation reaction as the dispersion of Au particles is greatly improved after Ce introduction, and the most active Au/CeM$_{imp}$ catalyst possesses the smallest Au particles. The primary explanation for gold particle size related to CO oxidation is that smaller gold particles possess more undercoordinated gold atoms, which are the vital active species for CO oxidation [3]. The second important factor influencing the catalytic response could be the interface between Au and Ce species. The recent study [40] reported that CO oxidation reaction readily occurred at perimeter sites between Au and oxide by the following process: (1) O_2 molecules were captured at the perimeter sites, and CO molecules on oxide sites were initially delivered to the active perimeter sites; (2) the O—O bond dissociated, and CO molecules reacted with oxygen at these perimeter sites. Due to the important role of Au—Ce interface in the reaction, different Au—Ce interfaces can induce distinct catalytic performance. For Au/CeM$_{imp}$ catalyst, the contact of Au and CeO_2 nanoparticles not only leads to continuous increase of Au—Ce contact boundaries but also modifies the chemical properties at such boundaries due to the presence of a larger number of oxygen vacancies at the surfaces of CeO_2 nanoparticles [41]. This contact can create a situation where oxygen can become readily activated and then move easily to react with the adsorbed CO molecules, due to that the increased Au—Ce contact junctions can minimize diffusion distance for the reactive surface species [42]. While for Au/CeM$_{ie}$ catalyst, the Au—Ce contact boundaries are limited due to that the Au—Ce contacts are between Au particles and Ce^{4+} (or Ce^{3+}) ions. Besides, as the absence of CeO_2 nanoparticles in Au/CeM$_{ie}$, the oxygen vacancies, which are crucial to active oxygen in the reaction process [43], are absent accordingly. Consequently, Au/CeM$_{imp}$ catalyst shows higher activity than Au/CeM$_{ie}$ one.

To clarify the essential role of Ce modification, these Au catalysts were pretreated by different streams, as shown in Fig. 7(b). Au/M sample, pretreated by either CO or O_2 stream, still shows no activity probably due to the inertness of bulk Au. For Au/CeM$_{imp}$ sample, both CO and O_2 pretreatments lead to a pronounced increase in activities compared with N_2 pretreatment, but no appreciable difference in the activities between CO and O_2 pretreatment is identified. For Au/CeM$_{ie}$ sample, the activities are ranked in the order Au/CeM$_{ie}$—O_2 > Au/CeM$_{ie}$—CO > Au/CeM$_{ie}$—N_2. Nevertheless, as pretreated by same gas, Au/CeM$_{imp}$ exhibits higher activity than Au/CeM$_{ie}$ one. As reported in literatures [44,45], CeO_2 nanoparticles with oxygen vacancies are able to adsorb and activate O_2, as well as provide channel to transport activated oxygen from ceria to metal nanoparticles, that is, oxygen reverse spillover, through the redox processes realized by Ce^{4+}/Ce^{3+} redox couple. Thus, with the unique oxygen releasing–uptaking property of CeO_2 nanoparticles, Au/CeM$_{imp}$ sample exhibits high activities in both CO and O_2 pretreatments. While for Au/CeM$_{ie}$ sample, redox cycles of Ce^{4+}/Ce^{3+} for isolated Ce ions in mordenite are possibly difficult to realize due to that the distances among Ce ions are adverse for charge transfer. This hypothesis can be proved in the corresponding parts of XPS results.

More important information can be obtained from the comparison of activities of three cycles and different stream pretreatments. For Au/CeM$_{imp}$ sample, the activities of the second and third cycle are approximate to the activities after CO and O_2

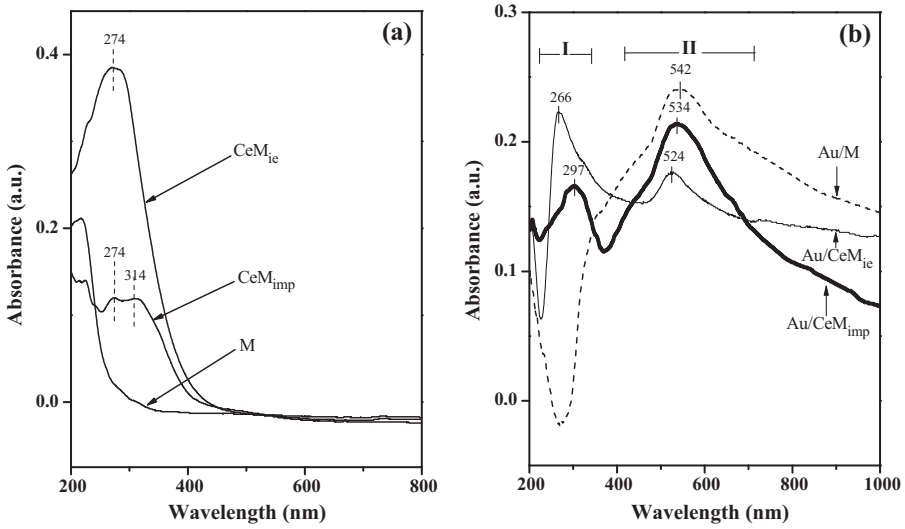

Fig. 4. UV–vis diffuse reflectance spectra of (a) supports and (b) Au catalysts.

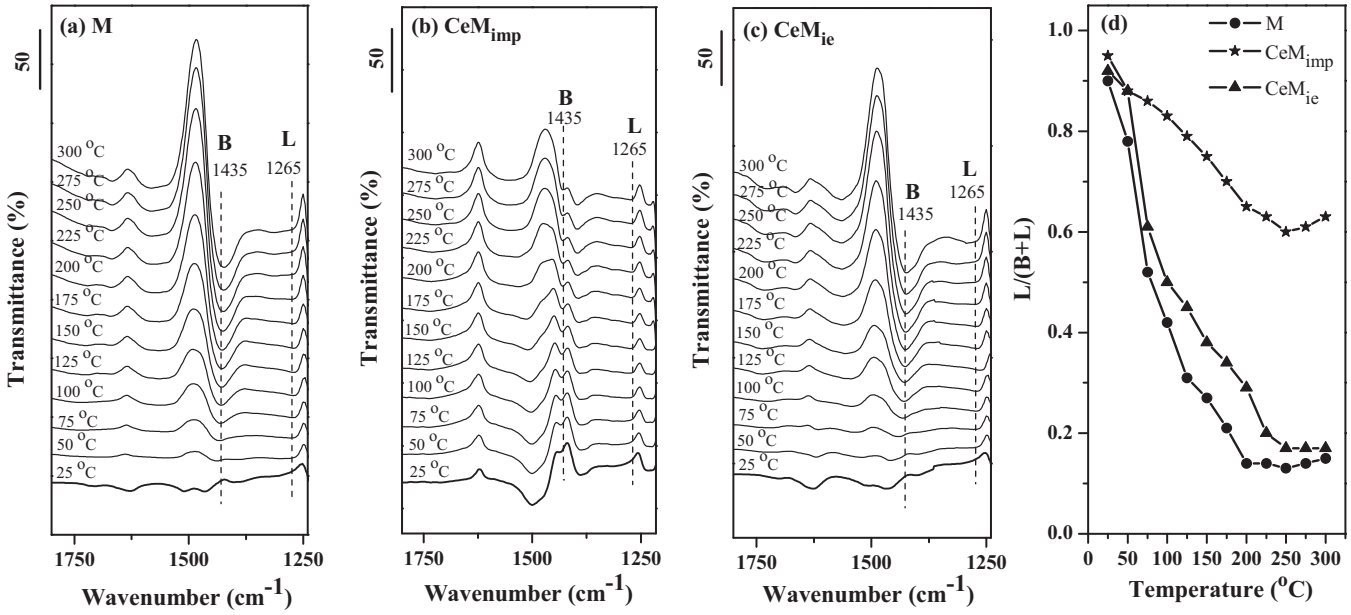

Fig. 5. NH_3 adsorption FT-IR results of supports: (a) M, (b) CeM_{imp}, (c) CeM_{ie}; (d) the percentage of Lewis acid sites in the total number of acid sites (Brønsted acid sites + Lewis acid sites) as a function of temperature.

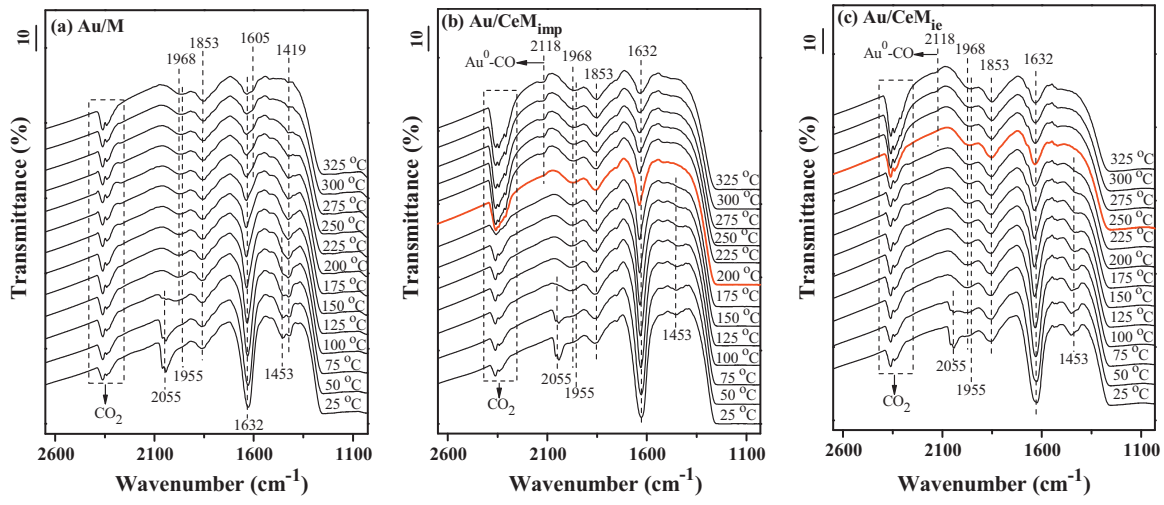

Fig. 6. In situ FT-IR spectra of CO adsorption on (a) Au/M, (b) Au/CeM_{imp} and (c) Au/CeM_{ie}.

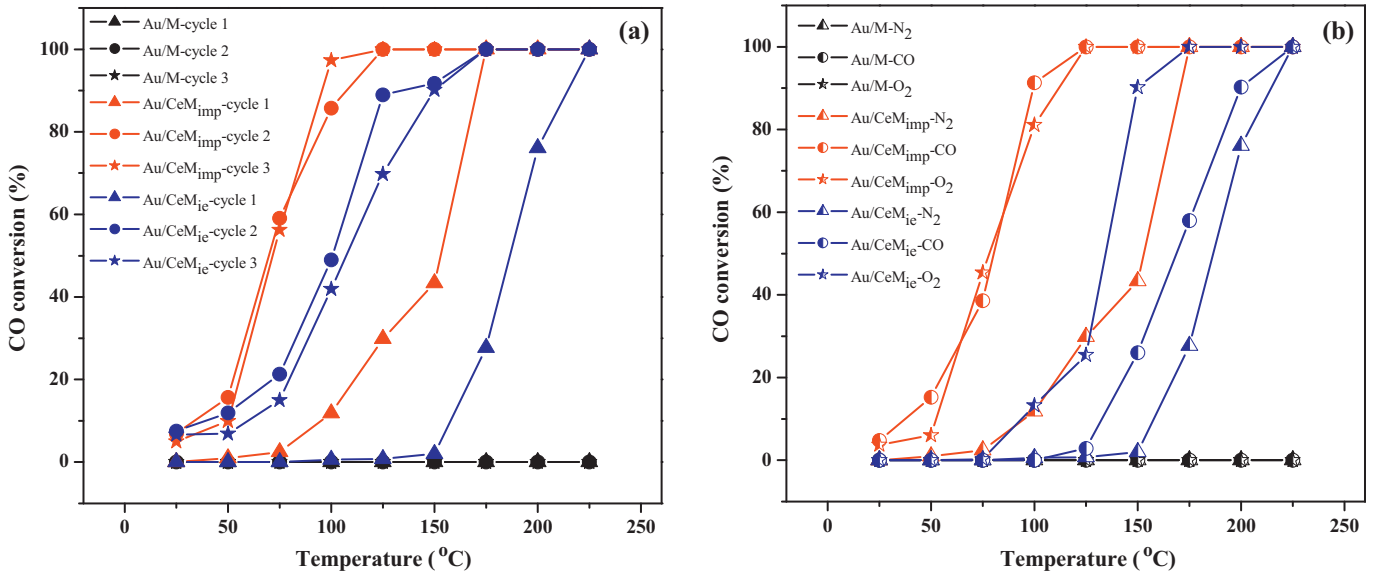

Fig. 7. CO conversion as a function of temperature over Au catalysts (a) for different catalytic cycles and (b) pretreated by different streams.

pretreatments, which are all higher than the activity of the first cycle or after N_2 pretreatment. For Au/CeM$_{ie}$ sample, the order of activities is as follows: Au/CeM$_{ie}$–cycle 2 > Au/CeM$_{ie}$–cycle 3 > Au/CeM$_{ie}$—O_2 > Au/CeM$_{ie}$—CO > Au/CeM$_{ie}$—N_2 (or Au/CeM$_{ie}$–cycle 1), which evidences that the mixture of CO and O_2 is more efficient to enhance the catalytic activity than CO or O_2 itself. These results can be rationalized by the assumption that the different synergistic effect between gold and cerium leads to different catalytic performance in CO and/or O_2 streams, as confirmed by XPS results below.

3.5. XPS results

XPS was performed in order to further investigate the influencing factors of CO oxidation activity for Au catalysts. The O 1s spectra (Fig. 8(a)) of fresh Au/M sample exhibit only one peak (O_I) at 532.2 eV, assigned to the surface adsorbed oxygen taking the forms of hydroxyl and carbonate species [46], and shows no significant modification after three catalytic operations. For Au/CeM$_{imp}$ and Au/CeM$_{ie}$ samples (Fig. 8(b) and (c)), the other O 1s peak (O_{II}) at 529.6 eV, corresponding to lattice oxygen [47], appears with the presence of cerium. The O_{II} intensities of spent Au/CeM$_{imp}$ samples are higher than those of spent Au/CeM$_{ie}$ ones, which indicates the existence of CeO_2 particles on Au/CeM$_{imp}$ sample. CeO_2 particles on Au/CeM$_{imp}$ possess higher oxygen storage–release capacity than Ce cations in Au/CeM$_{ie}$, which is effective for the promotion of reaction activity.

Au 4f spectra of Au catalysts after different catalytic cycles are shown in Fig. 8(d)–(f). In the freshly prepared Au catalysts, four peaks are found, which could be indexed to Au^0 ($Au4f_{7/2}$ and $Au4f_{5/2}$ located at 83.5 and 87.5 eV, respectively) and Au^{3+} ($Au4f_{7/2}$ and $Au4f_{5/2}$ observed at 85.0 and 88.5 eV, respectively) [48], suggesting the coexistence of Au^0 and Au^{3+} in these catalysts. The relative Au^{3+} content is estimated by the ratio of Au^{3+} area to the total area (denoted as [Au^{3+}]%), as shown in Fig. 10. Except for Au particle size and Au—Ce interface, the content of Au^{3+} is another important factor influencing the activity. Among these fresh Au catalysts, Au/CeM$_{imp}$ owns the highest ratio of Au^{3+} (15.1%) and exhibits the best activity. The significance of Au^{3+} content can be further evidenced by the catalytic performance in the three cycles of these catalysts. For Au/CeM$_{imp}$ catalysts (Fig. 10(a)), Au^{3+} content increases significantly after the first cycle of reaction, and subsequently the activity is further enhanced in the second run. The spent-2 catalyst, containing more Au^{3+}, still keeps the good catalytic performance in the third cycle. After three cycles, Au^{3+} content only shows slight increase in the spent-3 catalyst. For Au/CeM$_{ie}$ catalysts (Fig. 10(b)), the spent-1 catalyst has higher content of Au^{3+} than the fresh one, and consequently exhibits better catalytic performance than the fresh one. However, a decrease of Au^{3+} content is observed in the spent-2 catalyst, and subsequently the activity in the third cycle is depressed. Another fact, that Au/CeM$_{imp}$ catalyst contains more Au^{3+} and shows better catalytic performance than Au/CeM$_{ie}$ one in every cycle, can also prove the importance of Au^{3+} content in CO oxidation reaction. Thus, the content of Au^{3+} is closely related with the catalytic activity.

As shown in Fig. 8(g) and (h), the Ce 3d spectra are fitted with ten components and these peaks are denoted as v and u corresponding to Ce $3d_{5/2}$ and Ce $3d_{3/2}$ spin–orbit contributions, respectively. The peaks labeled v_0, v', u_0 and u' represent the presence of Ce^{3+}, while the peaks labeled v, v'', v''', u, u'' and u''' are characteristic of Ce^{4+} [49]. The semiquantitation of Ce^{3+} in the catalysts can be obtained by calculating the relative integrated area of u_0, u', v_0 and v' peaks to the total area of Ce 3d region, as shown in Eq. (1) [50]:

$$[Ce^{3+}]\% = \frac{100 \times [S(u_0) + S(u') + S(v_0) + S(v')]}{\sum[S(u) + S(v)]}\% \quad (1)$$

In the three cycles of CO oxidation reaction, the activities of Au/CeM$_{imp}$ gradually increase with Ce^{3+} content, while for Au/CeM$_{ie}$, the activity is enhanced in the second cycle as the Ce^{3+} content increases, and is suppressed in the third cycle with the decrease of Ce^{3+} content. Combined with Au 4f XPS results that Au^{3+} content increases with Ce^{3+} content in the three cycles, the role of ceria in this case would be to promote the formation of cationic Au^{3+} species by reducing partially Ce^{4+} to Ce^{3+} cations [51], which is the origin of Au—Ce synergistic effect [42]. Liu et al. [15] concluded from their DFT calculation that Au atom is oxidized by the interface Ce ion ($Au \rightarrow Au^{\delta+}$ and $Ce^{4+} \rightarrow Ce^{3+}$) even though there is no direct Ce—Au bonding. Their calculation showed that as a Au atom approached a surface O atom, the Au—O antibonding state evolved as a result of interaction between half-occupied 6s(Au) orbital and low-lying fully occupied 2p(O) orbital. The antibonding electron could tunnel into the nearby empty f(Ce) state, which became an electron reservoir in accepting or donating electrons. In this sense, the redox process between Au^0/Au^{3+} and

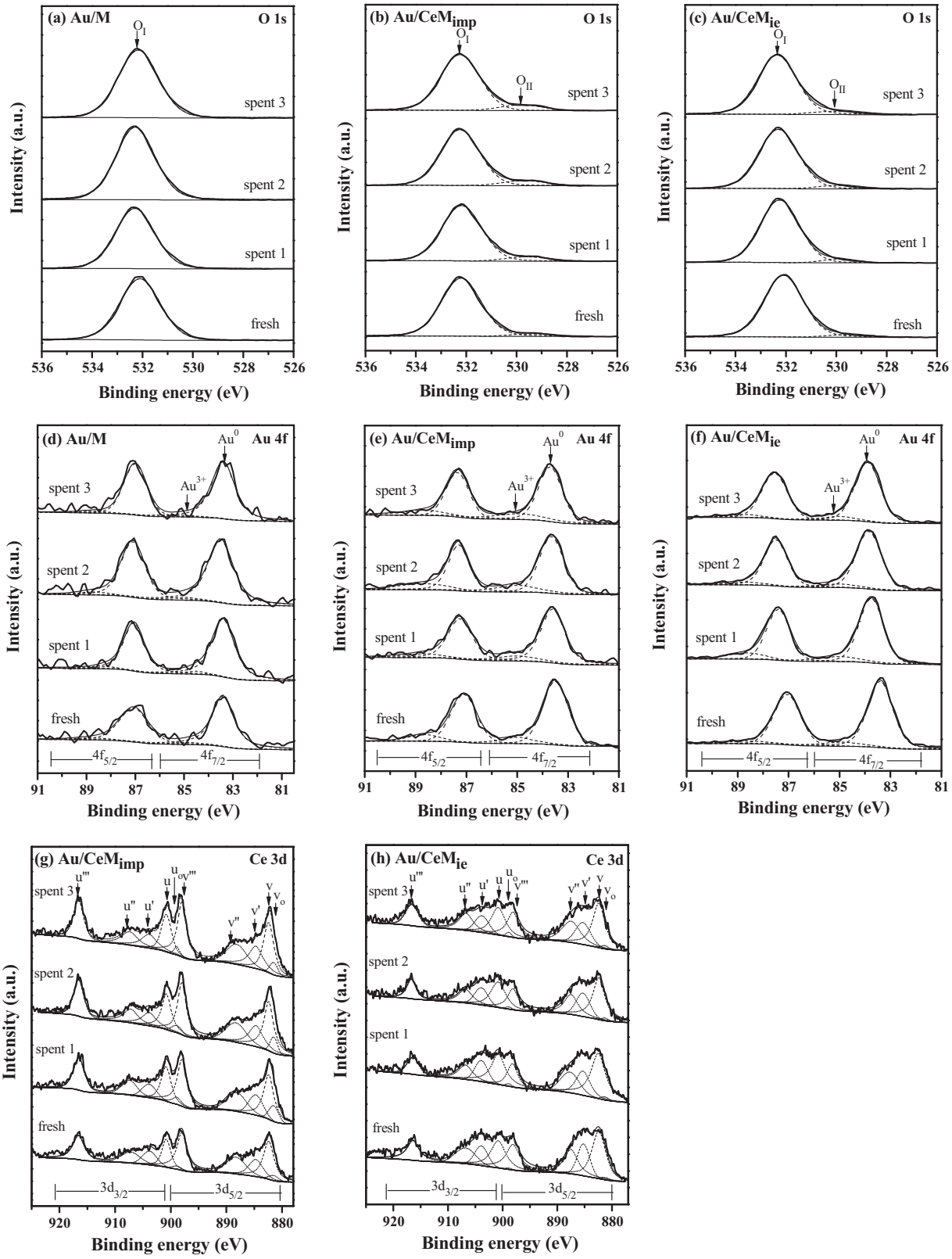

Fig. 8. XPS of Au catalysts for different catalytic cycles: (a–c) O 1s; (d–f) Au 4f; (g and h) Ce 3d.

Ce^{4+}/Ce^{3+} depends on the formation Au—O antibonding state. Compared with the interface of Au/CeM$_{imp}$ and Au/CeM$_{ie}$, Au—O antibonding state can be formed more readily on the interface between Au and CeO_2 particles of Au/CeM$_{imp}$ than on the interface between Au particles and Ce cations of Au/CeM$_{ie}$ due to the higher oxygen storage–release capacity of CeO_2 particles than Ce cations. Therefore, Au/CeM$_{imp}$ possesses higher ratios of Au^{3+} and Ce^{3+} than Au/CeM$_{ie}$, and shows better catalytic performance.

XPS results of these Au catalysts pretreated by different atmospheres are shown in Fig. 9. In the O 1s spectra

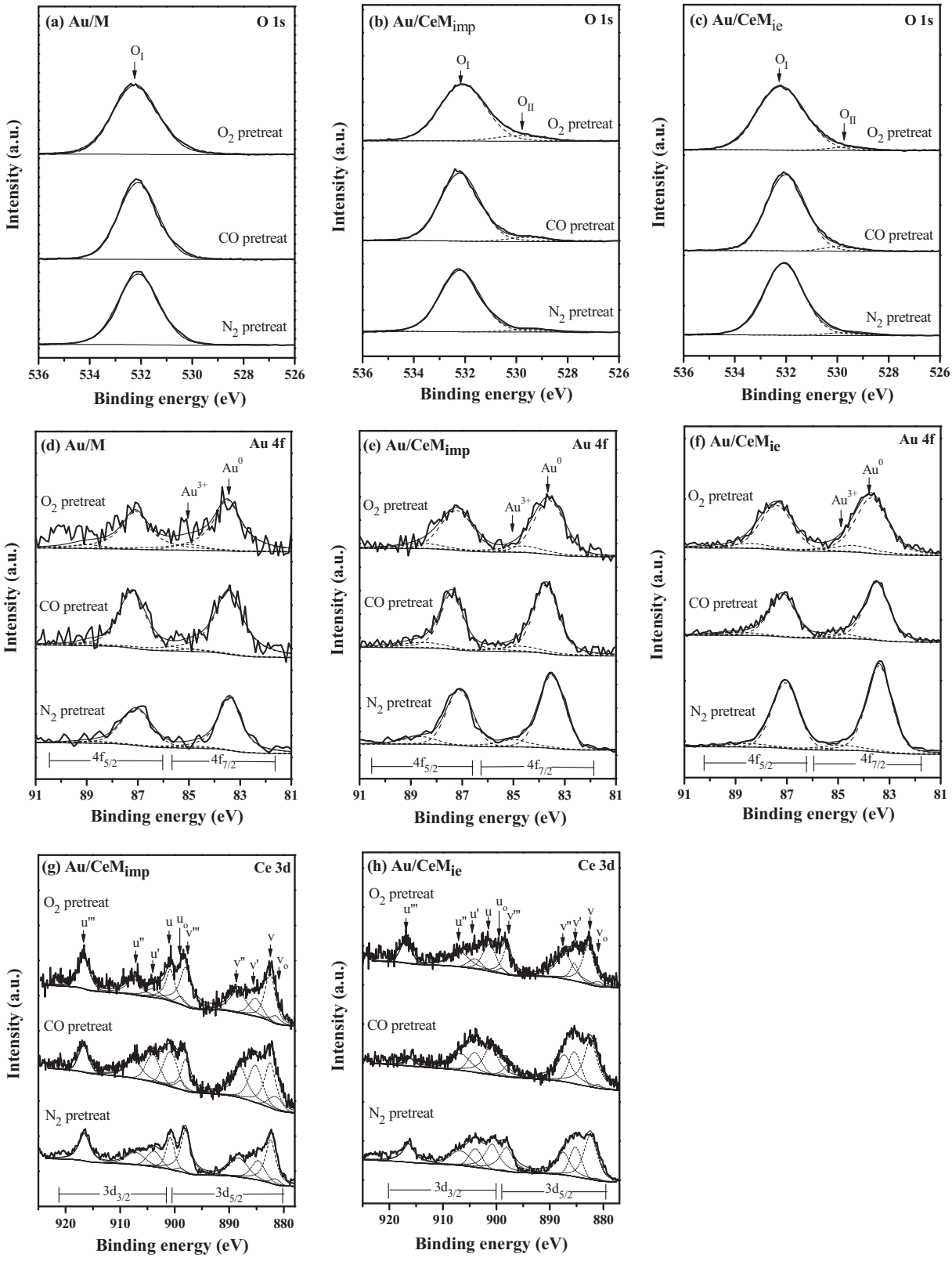

Fig. 9. XPS of Au catalysts pretreated by different streams: (a–c) O 1s; (d–f) Au 4f; (g and h) Ce 3d.

(Fig. 9(a)–(c)), Au/M samples exhibit one peak O_I at 532.2 eV attributed to the surface adsorbed oxygen [46], while for Au/CeM_{imp} and Au/CeM_{ie} samples, in addition to the main peak O_I, an apparent shoulder peak O_{II} at 529.6 eV representing the lattice oxygen is observed [47]. In the Au 4f spectra (Fig. 9(d)–(f)), the peaks corresponding to metallic gold (Au^0) and cationic gold (Au^{3+}), with Au $4f_{7/2}$ at 83.5 and 85 eV, respectively [48], could be resolved for all Au catalysts. As showed in the Ce 3d spectra (Fig. 9(g) and (h)), the characteristic peaks for Ce^{3+} (v_0, v', u_0 and u') and Ce^{4+} (v, v'',

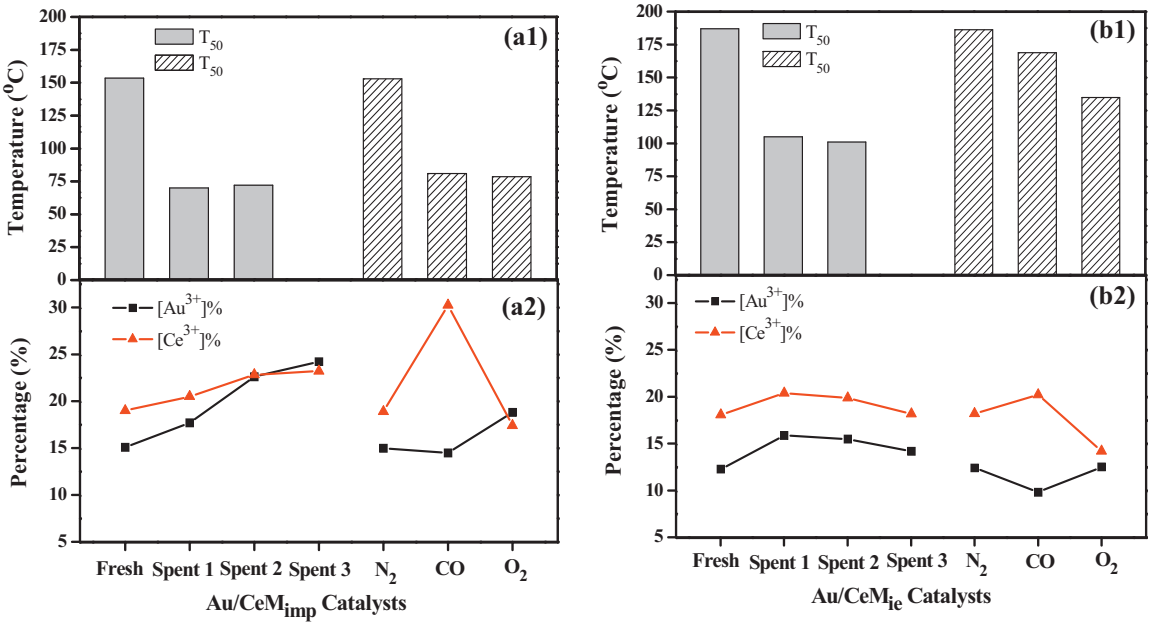

Fig. 10. The relation of surface chemical state and catalytic performance: (a1) T_{50} and (a2) [Au^{3+}]% and [Ce^{3+}]% of Au/CeM_{imp}; (b1) T_{50} and (b2) [Au^{3+}]% and [Ce^{3+}]% of Au/CeM_{ie} (T_{50}: the temperature of 50% CO conversion).

v''', u, u'' and u''') [49] are observed for the Ce-containing catalysts.

The relation between surface chemical state and catalytic performance of these Au catalysts pretreated by different streams is investigated, as shown in Fig. 10. For Au/CeM_{imp} sample (Fig. 10(a)), gold and cerium species can be reduced by CO stream, leading to the slight decrease of Au^{3+} ratio and the sharp increase of Ce^{3+} ratio compared with N_2 pretreatment. As Au/CeM_{imp} sample was pretreated by O_2 stream, compared with Au/CeM_{imp}—N_2, Au^{3+} ratio increases greatly, while Ce^{3+} ratio decreases slightly. These results indicate that CeO_2 particles possess the rapid redox cycle of Ce^{4+}/Ce^{3+} due to the oxygen storage–release capacity [42], which are beneficial for the improvement of activity. Moreover, Au/CeM_{imp}—CO has lower Au^{3+} ratio and higher Ce^{3+} ratio than Au/CeM_{imp}–spent 1 and Au/CeM_{imp}–spent 2, while Au^{3+} and Ce^{3+} ratios of Au/CeM_{imp}—O_2 are approximate to those of Au/CeM_{imp}–spent 1 and Au/CeM_{imp}–spent 2, which is one factor for Au/CeM_{imp}—CO and Au/CeM_{imp}—O_2 to exhibit comparable activity with Au/CeM_{imp}–spent 1 and Au/CeM_{imp}–spent 2. For Au/CeM_{ie} sample (Fig. 10(b)), CO pretreatment can increase Ce^{3+} ratio to 20.2%, higher than that pretreated by N_2. Au/CeM_{ie}—CO has comparable Ce^{3+} ratio with Au/CeM_{ie}–spent 1, but much lower Au^{3+} ratio. O_2 pretreatment can oxidize gold and cerium species and result in comparable Au^{3+} ratio but lower Ce^{3+} ratio compared with Au/CeM_{ie}–spent 1. Thus both Au/CeM_{ie}—CO and Au/CeM_{ie}—O_2 show lower activity than Au/CeM_{ie}–spent 1.

It should be noted that compared with N_2 pretreatment, Ce^{3+} ratio increases in a higher degree in Au/CeM_{imp}—CO sample than in Au/CeM_{ie}—CO one, and Au^{3+} ratio declines in a lower degree in Au/CeM_{imp}—CO sample than in Au/CeM_{ie}—CO one. These results can be rationalized by the fact that the contact of Au and CeO_2 particles is more favorable for charge transfer to form Ce^{3+} and Au^{3+} than that of Au particles and Ce cations. Although Au^{3+} in Au/CeM_{imp} sample is partially reduced by CO, the Au—Ce synergistic effect can provide a complement of Au^{3+} and consequently only a slight decrease of Au^{3+} is observed, which is difficult for Au/CeM_{ie} sample. This Au—Ce synergistic effect also plays an important role in the Ce-containing Au catalysts pretreated by O_2 stream. Compared with N_2 pretreatment, Au/CeM_{imp}—O_2 sample has a higher degree of increase in Au^{3+} ratio and a lower degree of decrease in Ce^{3+} ratio than Au/CeM_{ie}—O_2, which is due to the facile charge transfer on the interface between Au and CeO_2 particles to maintain adequate Au^{3+} and the oxygen storage–release capacity of CeO_2 particles to supply Ce^{3+}. Therefore, the Au—Ce synergistic effect on the interface between Au and CeO_2 particles is beneficial to improving the CO oxidation activities even after CO or O_2 pretreatment.

4. Conclusions

As demonstrated by comprehensive characterizations, the use of different methods of cerium modification leads to different properties of Au/CeM catalysts. Several major conclusions can be obtained as follows:

(1) Cerium introduction to Au supported mordenite material by ion-exchange method (Au/CeM_{ie}) produced interface between Au particles and Ce cations and showed better catalytic performance than the Ce-free one.
(2) A more superior performance than Au/CeM_{ie} is observed when Ce species are introduced by impregnation method on the mordenite support (Au/CeM_{imp}), and its highest performance is related to multiple factors:
   (i) the smallest size of Au particles are formed on the support surface with highest ratio of Lewis acid sites;
   (ii) a synergetic effect on the interface between Au and CeO_2 particles is enhanced by the facile redox of Ce^{4+}/Ce^{3+};
   (iii) the desorption or decomposition of carbonate species readily occurs.

Acknowledgements

The financial supports of the National Natural Science Foundation of China (No. 20973091), the National Basic Research Program of China (973 program, Nos. 2010CB732302, 2009CB623500) and Jiangsu Province Science and Technology Support Program (Industrial, BE2011167) are gratefully acknowledged.

References

[1] M. Haruta, N. Yamada, T. Kobayashi, S. Iijima, Journal of Catalysis 115 (1989) 301–309.
[2] M. Haruta, S. Tsubota, T. Kobayashi, H. Kageyama, M.J. Genet, B. Delmon, Journal of Catalysis 144 (1993) 175–192.
[3] B.K. Min, C.M. Friend, Chemical Reviews 107 (2007) 2709–2724.
[4] M.M. Schubert, S. Hackenberg, A.C.V. Veen, M. Muhler, V. Plzak, R.J. Behm, Journal of Catalysis 197 (2001) 113–122.
[5] A. Simakov, I. Tuzovskaya, N. Bogdanchikova, A. Pestryakov, M. Avalos, M.H. Farias, E. Smolentseva, Catalysis Communications 9 (2008) 1277–1281.
[6] J.H. Chen, J.N. Lin, Y.M. Kang, W.Y. Yu, C.N. Kuo, B.Z. Wan, Applied Catalysis A: General 291 (2005) 162–169.
[7] M.M. Mohamed, T.M. Salama, R. Ohnishi, M. Ichikawa, Langmuir 17 (2001) 5678–5684.
[8] J.N. Lin, J.H. Chen, C.Y. Hsiao, Y.M. Kang, B.Z. Wan, Applied Catalysis B: Environmental 36 (2002) 19–29.
[9] M.M. Mohamed, T.M. Salama, A.I. Othman, G.A. El-Shobaky, Applied Catalysis A: General 279 (2005) 23–33.
[10] T.M. Salama, I.O. Ali, M.M. Mohamed, Journal of Molecular Catalysis A: Chemical 273 (2007) 198–210.
[11] Y.J. Lee, G.H. He, A.J. Akey, R. Si, M. Flytzani-Stephanopoulos, I.P. Herman, Journal of the American Chemical Society 133 (2011) 12952–12955.
[12] T.M. Salama, M.M. Mohamed, I. Othman A, G.A. El-Shobaky, Applied Catalysis A: General 286 (2005) 85–95.
[13] M.F. Camellone, S. Fabris, Journal of the American Chemical Society 131 (2009) 10473–10483.
[14] H.Y. Kim, H.M. Lee, G. Henkelman, Journal of the American Chemical Society 134 (2012) 1560–1570.
[15] Z.P. Liu, S.J. Jenkins, D.A. King, Physical Review Letters 94 (2005) 196102-1–196102-4.
[16] Z. Zhou, S. Kooi, M. Flytzani-Stephanopoulos, H. Saltsburg, Advanced Functional Materials 18 (2008) 2801–2807.
[17] E.L. Pires, M.J.C. Ihaes, U. Chuhardt, Applied Catalysis A: General 203 (2000) 231–237.
[18] M. Lezcano, A. Ribotta, E. Miro, E. Lombardo, J. Petunchi, C. Moreaux, J.M. Dereppe, Journal of Catalysis 168 (1997) 511–521.
[19] P.C. van Geem, K.F.M.G.J. Scholle, G.P.M. van der Velden, W.S. Veeman, Journal of Physical Chemistry 92 (1988) 1585–1589.
[20] M.M. Mohamed, S.M.A. Katib, Microporous and Mesoporous Materials 93 (2006) 71–81.
[21] P. Castaño, T.A. Zepeda, B. Pawelec, M. Makkee, J.L.G. Fierro, Journal of Catalysis 267 (2009) 30–39.
[22] S.C. Laha, P. Mukherjee, S.R. Sainkar, R. Kumar, Journal of Catalysis 207 (2002) 213–223.
[23] I.V. Tuzovskaya, A.V. Simakov, A.N. Pestryakov, N.E. Bogdanchikova, V.V. Gurin, M.H. Farías, H.J. Tiznado, M. Avalos, Catalysis Communications 8 (2007) 977–980.
[24] J.A. Hernandez, S. Gómez, B. Pawelec, T.A. Zepeda, Applied Catalysis B: Environmental 89 (2009) 128–136.
[25] B. Lee, H. Zhu, Z. Zhang, S.H. Overbury, S. Dai, Microporous and Mesoporous Materials 70 (2004) 71–80.
[26] A.S. Mamede, E. Payen, P. Grange, G. Poncelet, A. Ion, M. Alifanti, V.I. Pârvulescu, Journal of Catalysis 223 (2004) 1–12.
[27] L. Chen, J.H. Li, M.F. Ge, Journal of Physical Chemistry C 113 (2009) 21177–21184.
[28] C.Z. Sun, L.H. Dong, W.J. Yu, L.C. Liu, H. Li, F. Gao, L. Dong, Y. Chen, Journal of Molecular Catalysis A: Chemical 346 (2011) 29–38.
[29] A. Gervasini, C. Messi, D. Flahaut, C. Guimon, Applied Catalysis A: General 367 (2009) 113–121.
[30] J.I. Villegas, D. Kubička, H. Karhu, H. Österholm, N. Kumar, T. Salmi, D.Y. Murzin, Journal of Molecular Catalysis A: Chemical 264 (2007) 192–201.
[31] X.N. Wang, Z. Zhao, C.M. Xu, A.J. Duan, L. Zhang, G.Y. Jiang, Journal of Rare Earths 25 (2007) 321–328.
[32] M.C.I. Bezen, C. Breitkopf, N.E. Kolli, J.M. Krafft, C. Louis, J.A. Lercher, Chemistry: A European Journal 17 (2011) 7095–7104.
[33] A.N. Pestryakov, A.A. Davydov, Applied Surface Science 103 (1996) 479–483.
[34] M. Baron, O. Bondarchuk, D. Stacchiola, S. Shaikhutdinov, H.J. Freund, Journal of Physical Chemistry C 113 (2009) 6042–6049.
[35] X.S. Huang, H. Sun, L.C. Wang, Y.M. Liu, K.N. Fan, Y. Cao, Applied Catalysis B: Environmental 90 (2009) 224–232.
[36] M. Kantcheva, O. Samarskaya, L. Ilieva, G. Pantaleo, A.M. Venezia, D. Andreeva, Applied Catalysis B: Environmental 88 (2009) 113–126.
[37] M. Sterrer, M. Yulikov, E. Fischbach, M. Heyde, H.P. Rust, G. Pacchioni, T. Risse, H.J. Freund, Angewandte Chemie International Edition 45 (2006) 2630–2632.
[38] M.M. Mohamed, M. Ichikawa, Journal of Colloid and Interface Science 232 (2000) 381–388.
[39] A. Penkova, K. Chakarova, O.H. Laguna, K. Hadjiivanov, F.R. Saria, M.A. Centeno, J.A. Odriozola, Catalysis Communications 10 (2009) 1196–1202.
[40] I.X. Green, W.J. Tang, M. Neurock, J.T. Yates Jr., Science 333 (2011) 736–739.
[41] D. Andreeva, M. Kantcheva, I. Ivanov, L. Ilieva, J.W. Sobczak, W. Lisowski, Catalysis Today 158 (2010) 69–77.
[42] M.A. Centeno, M. Paulis, M. Montes, J.A. Odriozola, Applied Catalysis A: General 234 (2002) 65–78.
[43] W.Y. Hernández, F. Romero-Sarria, M.A. Centeno, J.A. Odriozola, Journal of Physical Chemistry C 114 (2010) 10857–10865.
[44] S. Carrettin, P. Concepción, A. Corma, J.M.L. Nieto, V.F. Puntes, Angewandte Chemie International Edition 43 (2004) 2538–2540.
[45] G.N. Vayssilov, Y. Lykhach, A. Migani, T. Staudt, G.P. Petrova, N. Tsud, T. Skála, A. Bruix, F. Illas, K.C. Prince, V. Matolín, K.M. Neyman, J. Libuda, Nature Materials 10 (2011) 310–315.
[46] Y. Dai, X.Y. Wang, Q.G. Dai, D. Li, Applied Catalysis B: Environmental 111–112 (2012) 141–149.
[47] W.P. Shan, F.D. Liu, H. He, X.Y. Shi, C.B. Zhang, Applied Catalysis B: Environmental 115–116 (2012) 100–106.
[48] Z. Chen, Q.M. Gao, Applied Catalysis B: Environmental 84 (2008) 790–796.
[49] W.D. Cai, F. Chen, X.X. Shen, L.J. Chen, J.L. Zhang, Applied Catalysis B: Environmental 101 (2010) 160–168.
[50] J. Silvestre-Albero, F. Rodríguez-Reinose, A. Sepúlveda-Escribano, Journal of Catalysis 210 (2002) 127–136.
[51] N.J. Castellani, M.M. Branda, K.M. Neyman, F. Illas, Journal of Physical Chemistry C 113 (2009) 4948–4954.